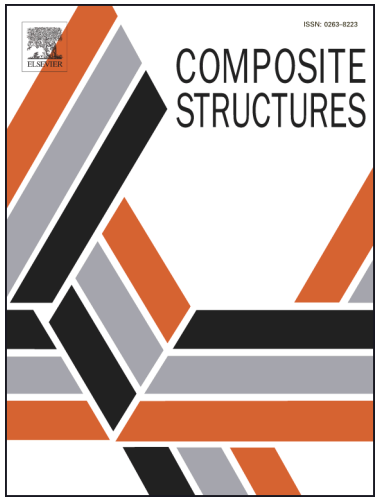

Finite Element Analysis of the Longitudinal Half Fixed Beam method for mode III characterization

Jorge Bonhomme, Victoria Mollón, Jaime Viña, Antonio Argüelles

PII: S0263-8223(19)32618-2
DOI: https://doi.org/10.1016/j.compstruct.2019.111546
Reference: COST 111546

To appear in: *Composite Structures*

Received Date: 11 July 2019
Revised Date: 26 September 2019
Accepted Date: 4 October 2019

Please cite this article as: Bonhomme, J., Mollón, V., Viña, J., Argüelles, A., Finite Element Analysis of the Longitudinal Half Fixed Beam method for mode III characterization, *Composite Structures* (2019), doi: https://doi.org/10.1016/j.compstruct.2019.111546

Finite Element Analysis of the Longitudinal Half Fixed Beam method for mode III characterization

Jorge Bonhomme[1], Victoria Mollón[2], Jaime Viña[2], Antonio Argüelles[1]

[1]Department of Construction and Manufacturing Engineering, University of Oviedo, Polytechnic School of Engineering, 33203 Gijón, Spain

[2]Department of Materials Science and Metallurgical Engineering, University of Oviedo, Polytechnic School of Engineering, 33203 Gijón, Spain

Abstract:

In this work, the Longitudinal Half Fixed Beam test (LHFB) for mode III characterization is analysed by means of Finite Element Analysis (FEA) and optical microscopy. The obtained results were compared with experimental data and analytical formulations obtained in previous works. The objective of this study is to determine the energy distribution across the crack front and to understand the micromechanics that give rise to the delamination failure in unidirectional carbon/epoxy composites.

It was found that for samples with long initial crack lengths (i.e. a_0=30 mm), pure mode III takes place in the central part of the delamination front. Nevertheless, these samples present a significant contribution of mode II at the edges of the specimen. As a_0 decreases, pure mode III increases in extension across the delamination front and mode II decreases at the sample edges. When the initial crack length (a_0) is quite small, the sample presents pure mode III practically on the entire length of the crack front. Nevertheless, when the initial crack is very small, the applied force exercises a local influence on the tip of the crack at the edge of the sample and mode III distribution loses its uniformity across the crack front.

The concordance between the analytical results and the numerical results obtained by the Finite Element Method (FEM) was variable depending on the length of the crack and if the comparison was made with G_{III} or G_T as reference.

Intralaminar cracks at approximately 45° with respect to the midplane were observed in planes perpendicular to the direction of delamination propagation (planes perpendicular to the fibre direction). Other authors also found this type of intralaminar cracks in other mode III test configurations.

Keywords: Mode III ; fracture ; delamination ; carbon-epoxy composites

1. Introduction:

Due to the laminated nature of composite materials, delamination is one of the main factors that limit the in service life of this type of materials. The onset and growth of cracks between plies can take place in three different ways: in opening mode (mode I), sliding mode (mode II) and tearing mode (mode III) (see Fig. 1).

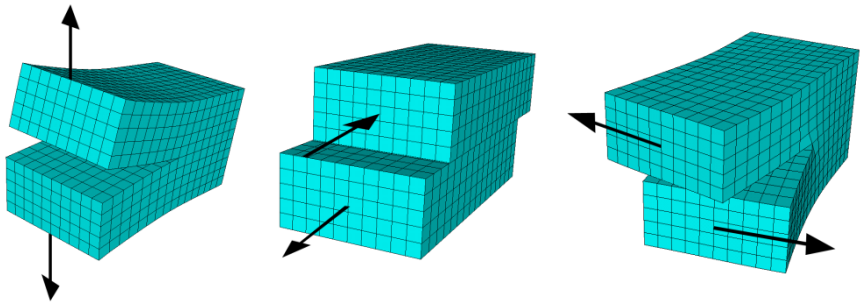

(a) Mode I (b) Mode II (c) Mode III

Fig. 1. Different crack opening modes.

Modes I and II have been widely studied by the scientific community [1], [2], [3], [4]. Mode I is usually characterized by means of the DCB test (Double Cantilever Beam). This test has been elevated to international standards [5], [6]. Mode II is usually characterised by means of the ENF test (End Notched Flexure). This test has been recently standardized by ASTM [7]. These test configurations produce pure and uniform modes I or II at the crack front.

In actual structures, we usually find mixed modes instead of pure modes. Modes I/II have been also widely studied [8], [9], [10] and there are large number of test methods that allow the determination of G_c (Energy Release Rate) as a function of different I/II mode ratios [11].

Conversely, pure mode III is more difficult to be reproduced by means of laboratory tests. There are also few works in the scientific literature regarding mixed modes including Mode III as I/III or II/III [12]

Despite these difficulties, there are some mechanical tests developed in the scientific literature in order to evaluate G_{IIIc} (mode III Energy Release Rate). One of the first mechanical tests developed was de Split Cantilever Beam (SCB) in 1988 by S.L. Donaldson [13] (see Fig. 2).

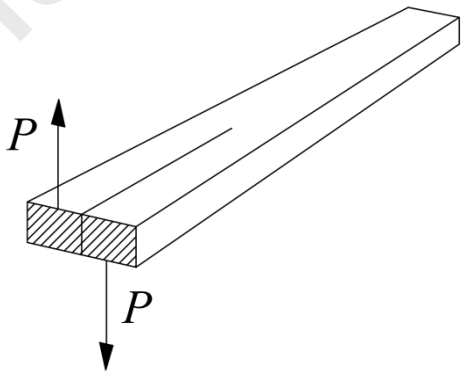

Fig. 2. Split Cantilever Beam (SCB) test.

In this test, the composite sample is bonded between aluminium bars in order to reduce arms bending.

Donaldson [13] found that for the shorter crack lengths, effects such as uneven load introduction, transverse shear strain, and crack tip rotation in the beam were dominant. When

analysing fracture surfaces, he found that the overall surface appearance did not change from the edge of the specimen to the centre, indicating that the stress state and the mode of failure was uniform across the specimen width (in contrast to R.H. Martin [14]). He also did not find any debris in the fracture surface concluding that frictional losses were negligible. Donaldson concluded that Mode II effects due to rotation were probably minimal. Nevertheless, he pointed out that a full 3D stress analysis of the specimen would be useful to determine mode I, II and III distribution across the crack front.

R.H. Martin [14] wrote a NASA technical memorandum in order to analyse this test configuration. Martin found that, although mode III is predominant, some degree of mode II was present. He found that G_{II} was higher than G_{III} near the free edges. He also found that, as the crack increased in length, G_{II}/G_{III} also increased. The presence of G_{II} at the edges was confirmed by observation of shear hackles and no fibre bridging in the delaminated surfaces [14]. At the centre of the sample, where mode III was predominant, significant fibre bridging was found. He finally concluded that SCB test do not properly reproduce pure mode III.

Martin determined that the possible cause for fibre bridging was the high stresses in planes perpendicular to the fibres. He found cracks ahead of the delamination front that could cause fibre bridging. These cracks could be produced due to high shear stresses in planes perpendicular to the fibres [14]. He concluded that this damage could cause the delamination to grow by joining the ends of the cracks.

Becht and Gillespie [15] developed a double Crack Rail Shear (CRS) test to measure G_{IIIc} (Fig. 3). They concluded that CRS was a viable specimen for measuring Mode III. Nevertheless, Martin [14] stated that this test configuration had very low compliance, and hence, accurate values of compliance and change in compliance with delamination growth were difficult to be obtained.

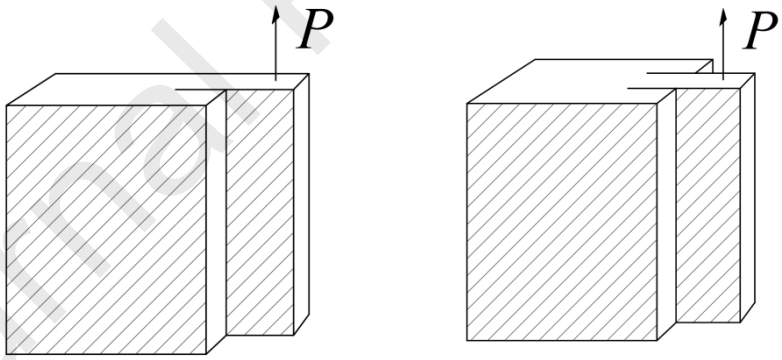

(a) Single Rail (b) Double rail

Fig. 3. Crack Rail Shear (CRS) test.

Another typical configuration to evaluate mode III is the Edge Crack Torsion test (ECT) (Fig. 4) [16], [17], [18].

The laminate specimen stacking sequence for this test is $[90/(+45/-45)_n/(-45/+45)_n/90]_s$, being 0° the direction parallel to the crack front. In this test configuration opposite moments are applied to the specimen ends.

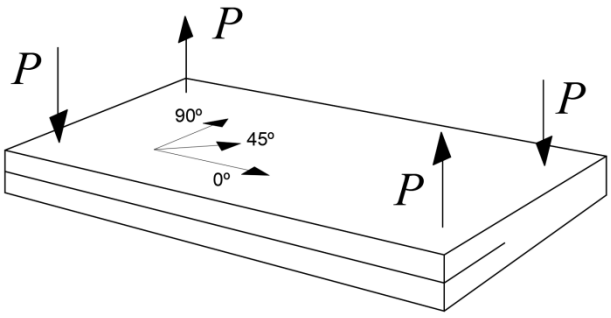

Fig. 4. Edge Crack Torsion Test (ECT).

In his analysis of the ECT test, Ratcliffe [19] found that the force versus deflection response deviated from linearity before the delamination growth onset. He attributed this deviation to the onset of localized delamination growth and splitting of the plies bounding the insert front. Czabaj et al. [20] found intralaminar cracks in the ECT samples. The orientation of these cracks was approximately 45° with respect to the midplane. They used ultrasonic inspection and optical microscopy. They found that delamination growth took place one ply interface beneath the midplane and that the delamination advance results from a coalescence of this angled intralaminar matrix cracks that extend to the midplane plies. They found that the initiation of these cracks took place prior to the nonlinearity point in the load versus displacement curve, or at the same time. They concluded that ECT test, due to these drawbacks, was unsuitable for characterizing the onset of mode III delamination.

Johnston et al. [21] also found these 45° micro-cracks in four split-beam-type tests analysed in their work.

Czabaj et al. developed a study of a modified ECT sample [22] where they tested different ply angles of the plies near the midplane trying to contain the intralaminar cracking arising from the crack front. They found that specimens with angles of 15° and 30° exhibited pure delamination extension without any other form of damage (no intralaminar cracking). Nevertheless, they found inconsistent results between both configurations.

Another test to determine mode III, named Edge Ring Crack Torsion (ERCT), have been developed by Ge et al. [23]. This test configuration is shown in Fig. 5. This test consists in a torsion test on a composite plate containing a circular crack (ring) between two layers.

They concluded that, in this test, the fracture process takes place in pure mode III without contribution of mode I or mode II component.

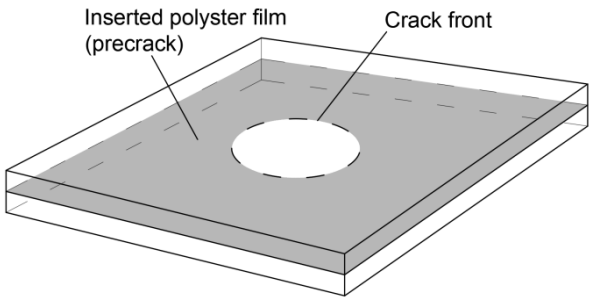

Fig. 5. Edge Ring Crack Torsion (ERCT).

López-Menéndez et al. [24], [25], [26], have recently developed a new test to evaluate mode III. This test configuration named Longitudinal Half Fixed Beam test (LHFB) is shown in Fig. 6.

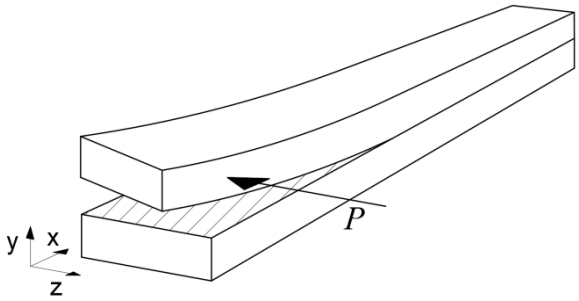

Fig. 6. Longitudinal Half Fixed Beam test (LHFB).

In this test, a load is applied by means of a torsional test machine to the upper half of a DCB sample with the bottom half fixed to the testing machine. A linear bearing allows the sample to move in the x direction in order to avoid forces in this axis.

In the present work, the LHFB test is analysed by means of Finite Element Method (FEM) in order to determine the mode III distribution across the delamination front. The contribution of modes I and II has also been determined. Finally, an analysis by means of optical microscopy was carried out in order to study damage evolution across the crack front.

In order to compare results, a previous experimental program [24] carried out with samples of AS4/8552 unidirectional carbon/epoxy laminates with different initial crack lengths was taken as reference.

2. FEM model

An ANSYS® 19.0 Academic Research package was used in order to perform the FEM analysis. Some models were prepared in order to find the optimal element size. The mesh was refined near interesting areas as sample edges and crack front (Fig. 7). The element used was the 3D structural SOLID45.

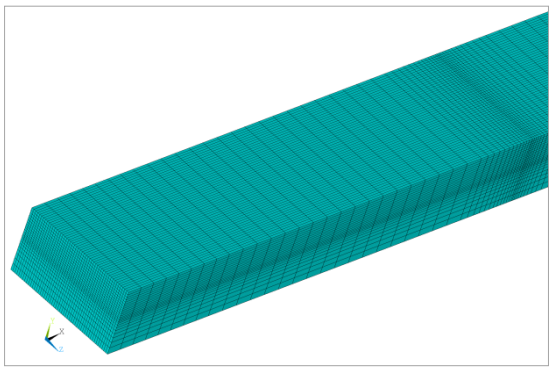

Fig. 7. Mesh with refined areas.

In order to model the boundary conditions, two different cases were studied. First, faces A, B, C and D were constrained to move in the z direction. The bottom face of the sample was constrained in the y direction (Fig. 8). This model was named “model 1”.

Nevertheless, sample faces are simply supported in the testing machine. They are not bonded to the testing tool (Fig. 9). Therefore, in a second study, only faces A and C were constrained in the z direction (faces that are compressed against the testing tool during the test). This second model was named “model 2”.

A more realistic approach would involve the modelling of the testing tool and the use of contact elements between the sample and testing tools. Nevertheless, this option was discarded as it would imply longer computing times, and it was also expected little improvement in the accuracy of the results.

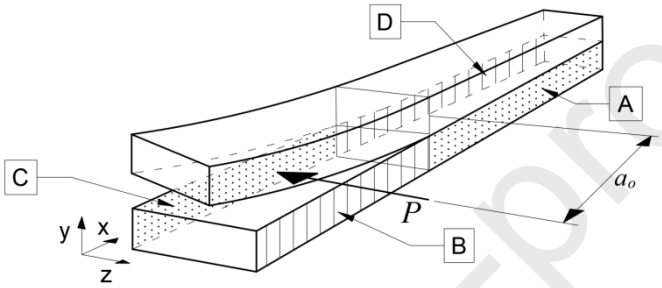

Fig. 8. Boundary conditions.

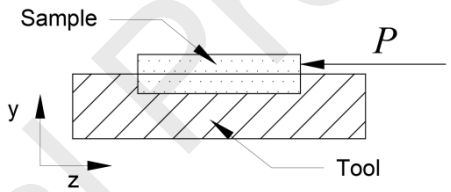

Fig. 9. Test configuration. Cross section.

In order to compute the energy release rate in modes I, II and III, the Two Step Crack Extension Method was used. In this method loads and displacements are calculated in the same node pairs at the crack tip (nodes *1i-1i'* in Fig. 10) [27][28][29]. As can be seen in Fig. 10, loads are calculated in the first step and the corresponding displacements are calculated in a second step once the nodes have separated. G_I, G_{II} and G_{III} are calculated by means of Eqs. (1).

This procedure is similar to the VCCT (Virtual Crack Closure Technique) [27], where forces and displacements are calculated in the same step (second step): forces area calculated in nodes *2i-2i'* and displacements in *1i-1i'*. This approximation is valid providing that forces in the crack front before and after the crack extension are similar when the crack increment (element size) is small enough.

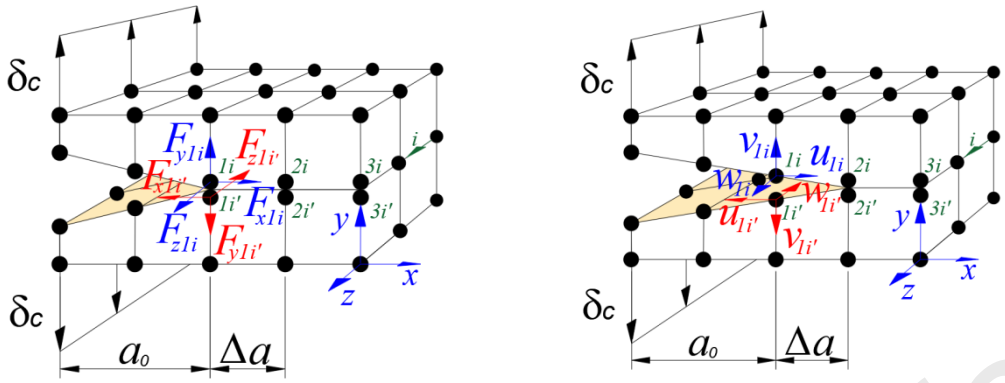

(a) Step 1 (b) Step 2

Fig. 10. FEM procedure for G_I, G_{II}, and G_{III}, determination.

$$G_I = \frac{1}{2B\Delta a}\sum_{i=1}^{n} F_{y1i}(v_{1i} - v_{1'i})$$

$$G_{II} = \frac{1}{2B\Delta a}\sum_{i=1}^{n} F_{x1i}(u_{1i} - u_{1'i})$$

$$G_{III} = \frac{1}{2B\Delta a}\sum_{i=1}^{n} F_{z1i}(w_{1i} - w_{1'i}) \quad (1)$$

B is the sample width. Other parameters are shown in Fig. 10.

Fig. 10 represents a DCB test. Nevertheless, the procedure can be extrapolated to any type of delamination test in modes I, II or III.

The element size ahead of the crack tip (where the crack opening takes place) was set to 0.136 mm for all samples (Fig. 11).

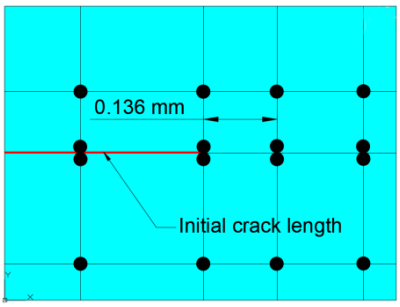

Fig. 11. Elements ahead of the crack tip.

The critical energy release rates given by Eqs. (1) are the sum of the work done by all the nodes of the crack front divided by the delaminated area ($B\Delta a$). This is equivalent to calculate the mean value of G_I, G_{II} and G_{III} across the crack front.

In order to evaluate the suitability of this test procedure, it is interesting to evaluate the distribution of G_I, G_{II} and G_{III} across the delamination front to check the uniformity of these distributions and the possible presence of mixed modes.

When analysing the variation of the energy release rate across the delamination front, we can use a procedure similar to that shown by R. Krueger [27] where the work done in each node is divided by the element width b (Fig. 12). In this figure, for simplicity, only two dimensions are shown and only the displacements in nodes 11 and 14 are represented.

In the procedure used in [27] forces and displacements are calculated in the second step (VCCT) in two consecutive node pairs. As mention above, this simplification assumes that the force at the crack tip changes shortly before and after the growth of the crack when the size of the element is sufficiently small. In the present work, no simplification is applied, and so, forces and displacements are calculated in the same node pair in two different steps (the nodes that separate when the crack extends Δa).

Therefore, in this work the value of the energy release rate at node i is calculated as:

$$G_{Ii} = \frac{1}{2b\Delta a} F_{y1i}(v_{1i} - v_{1'i}) = \frac{1}{2b\Delta a} F_{y1i}\delta v_{1i}$$

$$G_{IIi} = \frac{1}{2b\Delta a} F_{x1i}(u_{1i} - u_{1'i}) = \frac{1}{2b\Delta a} F_{x1i}\delta u_{1i}$$

$$G_{IIIi} = \frac{1}{2b\Delta a} F_{z1i}(w_{1i} - w_{1'i}) = \frac{1}{2b\Delta a} F_{z1i}\delta w_{1i} \tag{2}$$

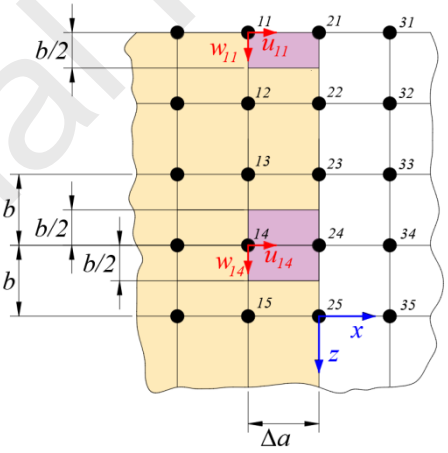

Fig. 12. FEM procedure to determine G_I, G_{II}, and G_{III}, distribution across the delamination front. For simplicity, only two dimensions and displacements in nodes 11 and 14 are shown.

The work done by the edge nodes was divided by $b/2$. The average value across the crack front calculated in this way is not exactly coincident with Eqs. (1). For example, the average value of G_{III} is:

$$G_{III} = \frac{1}{(2\Delta a)n}\left[\frac{F_{z11}\delta w_{11}}{b/2} + \frac{F_{z12}\delta w_{12}}{b} + \ldots + \frac{F_{z1n-1}\delta w_{1n-1}}{b} + \frac{F_{z1n}\delta w_{1n}}{b/2}\right]$$

$$G_{III} = \frac{1}{2nb\Delta a}\left[F_{z11}\delta w_{11} + F_{z1n}\delta w_{1n} + \sum_{i=1}^{n} F_{z1i}\delta w_{1i}\right]$$

(3)

Being n the number of nodes across the crack front and:

$$B = (n-1)b$$

(4)

As mention above, B is the sample width and b the element width. Nodes are supposed to be equally spaced.

The average value of G_I and G_{II} are calculated in a similar way.

First, a FEM model with n=31 nodes across the crack front and initial crack length a_0=30 mm was prepared. In this model, the difference between the average values obtained by means of Eqs. (3) and (1) was 4.9%. This model had an element width of 0.33 mm (b/B=0.033). If the element width is reduced by half (the number of nodes increased to n=61 and so the ratio b/B reduced to 0.017) the difference between Eqs. (3) and (1) is reduced to 0.2%. Nevertheless, the distributions of G_I, G_{II} and G_{III} across the crack front was practically the same in both cases. Furthermore, the total energy only changes 0.2%. Finally, a model with n=51 nodes across the crack front (b/B=0.02) was used for the analysis of all the models. This last model gave a maximum error of 3% between Eqs (1) and (3).

Another way to evaluate the variation of G_I, G_{II} and G_{III} across the crack front can be obtained by evaluating these values in each element. This procedure is shown in Fig. 13. For simplicity, in this figure only individual nodes are represented in the crack front. We must remember that in this FEM procedure there are pairs of coupled nodes placed in the crack front (each belonging to each sublaminate) that separates when the crack extends Δa.

In order to calculate G_{Ii}, G_{IIi} and G_{IIIi} in the crack front between nodes i and i+1 the forces used are the nodal forces in these nodes calculated with elements 1 and 2 (upper sublaminate) (see Fig. 13). In a similar way, to evaluate G_{Ii+1}, G_{IIi+1} and G_{IIIi+1} in the crack front between nodes i+1 and i+2 the forces are calculated taking into account elements 5 and 6 (see Fig. 13). The total forces in node i+1 corresponding to the upper sublaminate are: $F_{xi+1}+F'_{xi+1}$, $F_{yi+1}+F'_{yi+1}$, and $F_{zi+1}+F'_{zi+1}$.

G_{Ii}, G_{IIi} and G_{IIIi} are then calculated between nodes i and i+1 as follows:

$$G_{Ii} = \frac{1}{2b\Delta a}\left(F'_{yi}\delta v_i + F_{yi+1}\delta v_{i+1}\right)$$

$$G_{IIi} = \frac{1}{2b\Delta a}\left(F'_{xi}\delta u_i + F_{xi+1}\delta u_{i+1}\right)$$

$$G_{IIIi} = \frac{1}{2b\Delta a}\left(F'_{zi}\delta w_i + F_{zi+1}\delta w_{i+1}\right)$$

(5)

The average values of G_I, G_{II} and G_{III} distributions across the crack front calculated with this last procedure are equivalent to those obtained with Eqs. (1).

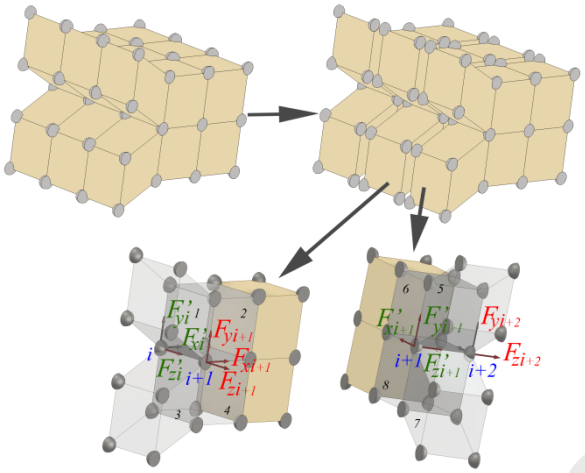

Fig. 13. FEM procedure to calculate G_{Ii}, G_{IIi} and G_{IIIi} between nodes i and $i+1$

3. Experimental procedure

An experimental program developed in previous works [24] has been taken as a reference to compare FEM results. In those works, two different unidirectional carbon/epoxy laminates were tested: AS4/8552 and AS4/3501-6. As both laminates gave rise to similar conclusions, only the results corresponding to AS4/8552 are used in this work.

The nominal dimensions of the samples used in the experimental program were as follows (Fig. 14):

- Length (L): 160-200 mm
- Width (B): 10 mm
- Thickness ($2h$): 6 mm

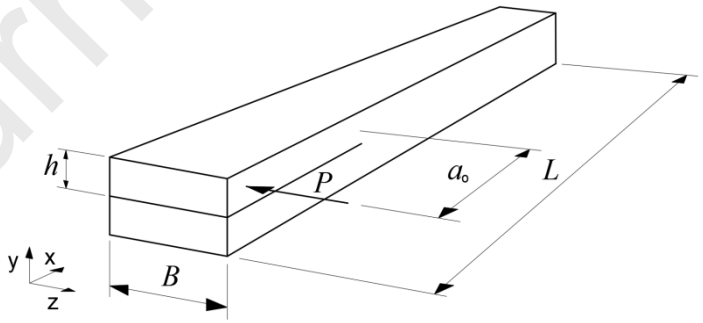

Fig. 14. Sample dimensions.

These samples were prepared with different crack lengths: 1, 5, 10, 15, 20, 26 and 30 mm. All samples had the same stacking sequence $[0°]_n$.

The mechanical properties of this laminate used to compute the analytical calculations and as input in the FEM models are shown in Table 1.

Property	AS4/8552
E_x (MPa)	144,000
E_y (MPa)	10,600
E_z (MPa)	10,600
G_{xy} (MPa)	5,360
G_{xz} (MPa)	5,360
G_{yz} (MPa)	3,786

Table 1. Mechanical properties of laminate AS4/8552.
E_i (tensile modulus), G_{ij} (shear modulus)

In order to calculate G, the following analytical expression based on the Timoshenko beam theory was used following references [14] and [24] :

$$G = \frac{1}{B}\left(\frac{P^2a^2}{2E_xI} + \frac{3P^2}{4BhG_s}\right) \tag{6}$$

Being $G_s = G_{xy} = G_{xz}$

4. Results and discussion

FEM models with two different boundary conditions were prepared as mentioned previously. In a first model (model 1) the movement in the *z* direction of faces A, B, C and D were constrained (Fig. 8). In a second model (model 2), only faces A and C were constrained in the *z* direction. As mention above, the material used was AS4/8552. Results obtained from the FEM calculations are shown in Tables 2 and 3. These results correspond to the critical values at the onset of the crack propagation calculated from the critical loads obtained experimentally in reference [24].

a_0 (mm)	G_I	G_{II}	G_{III}	G_T	G_I/G_T	G_{II}/G_T	G_{III}/G_T
30	7.3	422.9	873.1	1,303.3	1%	32%	67%
26	5.6	425.3	1,010.8	1,441.7	0%	30%	70%
20	5.1	298.8	891.8	1,195.6	0%	25%	75%
15	8.1	264.4	1,088.7	1,361.2	1%	19%	80%
10	10.8	159.8	1,020.9	1,191.5	1%	13%	86%
5	20.8	73.6	955.4	1,049.8	2%	7%	91%
1	22.1	26.2	1,345.8	1,394.0	2%	2%	97%

Table 2. Energy release rate in modes I, II and III calculated by FEM (J/m^2). Model 1.

a_0 (mm)	G_I	G_{II}	G_{III}	G_T	G_I/G_T	G_{II}/G_T	G_{III}/G_T
30	8.3	432.7	902.4	1,317.6	1%	33%	68%
26	7.1	433.2	1,041.4	1,457.2	0%	30%	71%
20	6.1	307.2	929.5	1,215.6	1%	25%	76%
15	9.4	273.2	1,141.9	1,390.0	1%	20%	82%
10	13.5	166.6	1,078.2	1,220.6	1%	14%	88%
5	25.2	78.2	1,013.9	1,049.0	2%	7%	97%
1	29.1	27.1	1,345.7	1,393.3	2%	2%	97%

Table 3. Energy release rate in modes I, II and III calculated by FEM (J/m^2). Model 2.

As can be seen in these Tables, there are no significant differences between both models. Model 1 furnishes slightly lower G_{III} values than model 2.

Fig. 15 show the distribution of G_I, G_{II} and G_{III} across the crack front as a function of the normalized width (z/B) for the sample with a_0=30. This figure compares the distribution of G_I, G_{II} and G_{III} based on nodal and element values (Eqs. (2) and (5)). As can be seen, both distributions are equivalent. Nodal values are higher at the edges. In this figure, element values are represented at the centre of the element.

Figs. 16 to 18 show the distribution of G_I, G_{II} and G_{III} across the crack front as a function of the normalized width (z/B) for different initial crack lengths (a_0=10, 5 and 1 mm) based on nodal values (results were obtained solving model 1). As can be seen, the curves are symmetric for long initial cracks (Figs. 15 and 16 with a_0=30 and 10 mm). Nevertheless, as the initial crack length decreases, the symmetry of the curves is lost (Figs. 17 and 18 with a_0=5 and 1 mm). This behaviour shows that, when the crack is very small, the applied force exercises a local influence on the tip of the crack at the edge of the sample where the force is applied and mode III distribution loses its uniformity across the crack front. In this case, G_{III} increases in the edge were the load is applied.

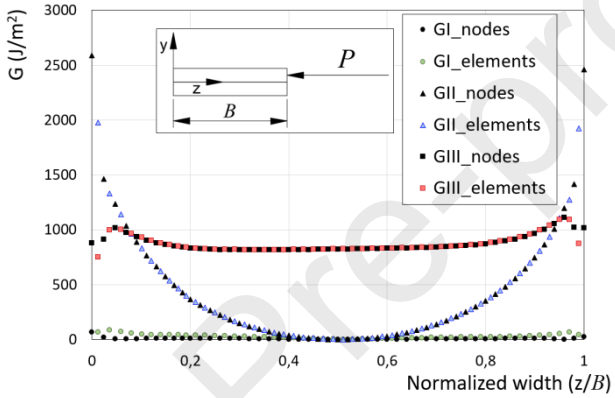

Fig. 15. a_0=30 mm. Model 1. G_I, G_{II} and G_{III} versus normalized width z/B.

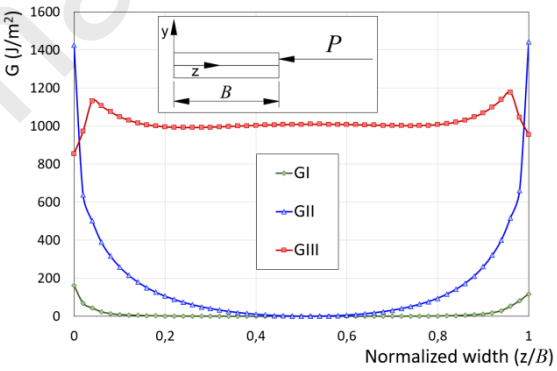

Fig. 16. a_0=10 mm. Model 1. G_I, G_{II} and G_{III} versus normalized width z/B

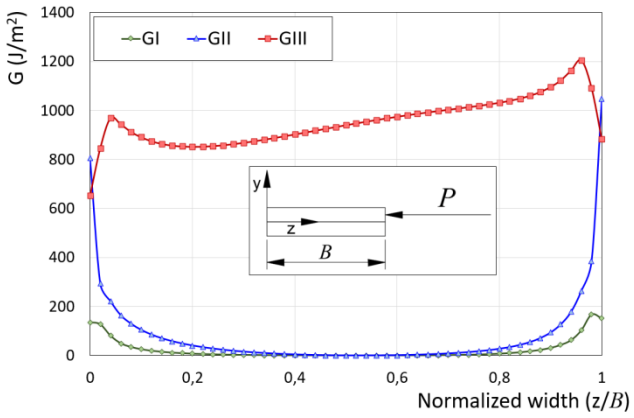

Fig. 17. a_0=5 mm. Model 1. G_I, G_{II} and G_{III} versus normalized width z/B

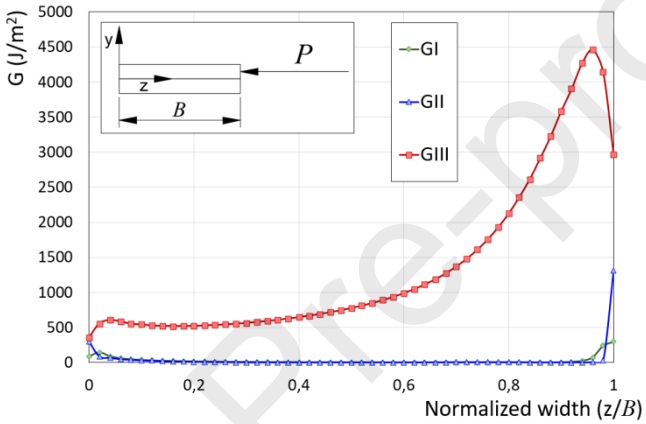

Fig. 18. a_0=1 mm. Model 1. G_I, G_{II} and G_{III} versus normalized width z/B

In samples with a_0=30 mm, pure mode III takes place only in the central part of the sample. In this sample there is a significant mode II contribution near the sample edges. As a_0 decreases, pure mode III distribution increases in extension. For a_0=10 mm pure mode III extends between z/b=0.4 and z/b=0.6. When the crack length is set to a_0=5 mm, this zone is placed between z/b=0.3 and z/b=0.7. Moreover, when a_0=1 mm, there is pure mode III practically on the entire length of the crack front.

As the load is applied closer to the crack tip, the bending moment decreases and, therefore, mode II contribution also decreases. Nevertheless, as mention above, when the load is applied too close to the crack tip, mode III distribution loses its uniformity across the crack front.

Finally, Mode I is practically negligible in all cases.

Fig. 19 and 20 show the distribution of G_{II} and G_{III} across the crack front for different initial crack lengths.

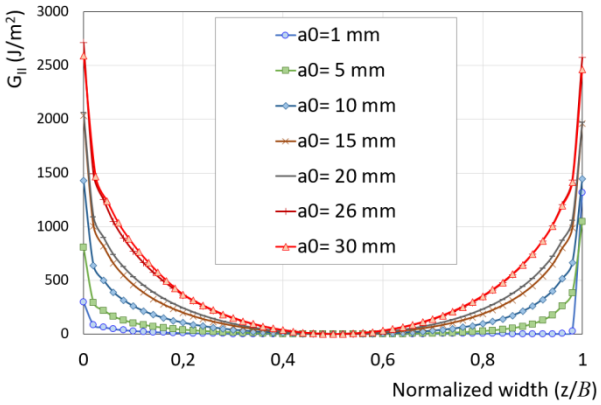

Fig. 19. G_{II} across the crack front for different initial crack lengths. Model 1.

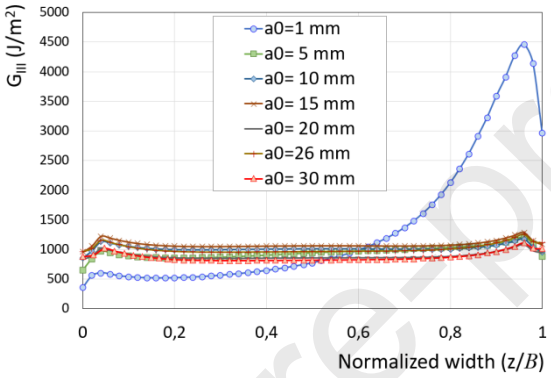

Fig. 20. G_{III} across the crack front for different initial crack lengths. Model 1.

As can be seen in Fig. 19, there are always some degree of mode II at the sample edges, but this contribution decreases as a_0 decreases. G_{II} is practically negligible for a_0 =1mm.

As can be seen in Fig. 20, G_{III} distribution shows little variation with a_0 and is uniform across the crack front for long initial crack lengths. For a_0=1 mm there is a sharp G_{III} peak near the edge where the load is applied denoting that local effects have great influence in this case.

Fig. 21 shows the ratios G_{II}/G_T and G_{III}/G_T (being $G_T=G_I+G_{II}+G_{III}$) across the crack front for different crack lengths using model 1.

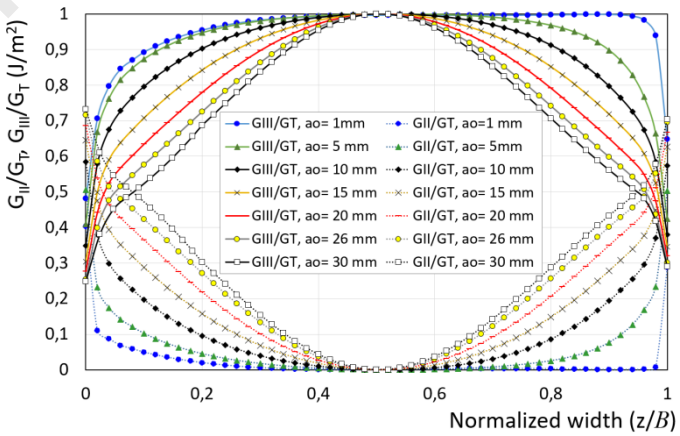

Fig. 21. G_{II}/G_T and G_{III}/G_T for different initial crack lengths. Model 1. AS4/8552.

Fig. 22 shows the critical results (G_{IIIc}) obtained by means of FEM for different initial crack lengths (a_0). As can be seen in this figure, G_{IIIc} seems to have a slight tendency to increase as the initial crack length decreases.

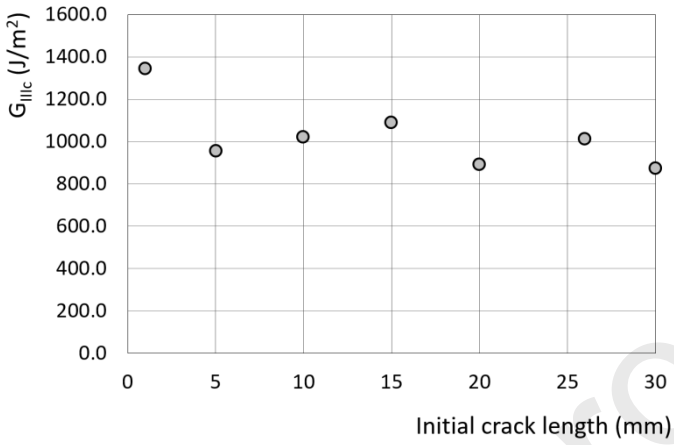

Fig. 22. G_{III} versus initial crack length.

Similar results were obtained with model 2. In this model the lateral faces have fewer constrains so the degree of symmetry in the graph is slightly lower (see Fig. 23 compared to Fig. 15). Nevertheless, the average value of G_{III} across the crack tip gives similar results.

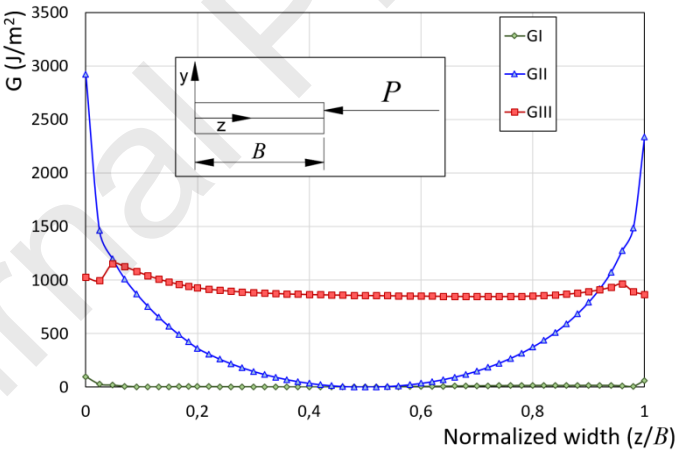

Fig. 23. a_0=30 mm. Model 2. AS4/8552.

The actual behaviour of the material is expected to be between models 1 and 2.

Table 4 shows the comparison between the analytical results calculated by means of Eq. (6) and those obtained by FEM.

a_0 (mm)	G_{III} (FEM)	G_T (FEM)	G (Analytical)	Error (G_{III} FEM-Analytical)	Error (G_T FEM-Analytical)
30	873.1	1,303.3	840.2	-4%	-36%
26	1,010.8	1,441.7	901.2	-11%	-37%
20	891.8	1,195.6	740.6	-17%	-38%
15	1,088.7	1,361.2	847.9	-22%	-38%
10	1,020.9	1,191.5	795.9	-22%	-33%
5	955.4	1,049.8	868.2	-9%	-17%
1	1,345.8	1,394.0	1,299.8	-3%	-7%

Table 4. Comparison between analytical and FEM results. Model 1 (J/m^2)

The analytical formulation takes into account the total energy involved in the test. This analytical formulation does not discriminate the different modes of fracture when mixed mode is present.

When comparing these results with the total energy G_T obtained by FEM, the error between results is in the order of 33-36% for a_0 between 10 and 30mm. It must be taken into account that for initial crack lengths between 15 and 30 mm the average mode II contribution is in the range of 20-30% of the total energy. The error decreases to 17-7% as the initial crack length decreases to 5-1 mm. For small initial crack lengths, the average contribution of mode II decreases to less than 10% and so, G_T is nearly coincident with G_{III}. Mode I contribution is always negligible.

When comparing G analytical with G_{III} obtained by FEM, results were closer (4-23%) (see Table 4).

5. Microscopy Analysis:

Samples tested in previous works [24] were prepared and observed in transversal planes (planes parallel to yz plane) by means of an optical microscope. Fig. 24 shows a drawing with the numbered sections observed in the microscope. Section 1 is a section ahead of the initial crack front. Section 2 is a section slightly behind the initial crack front and section 3 represents a cut behind section 2. Fig. 25 shows a micrograph of section 2 of the upper sublaminate of a sample with a_0=20 mm.

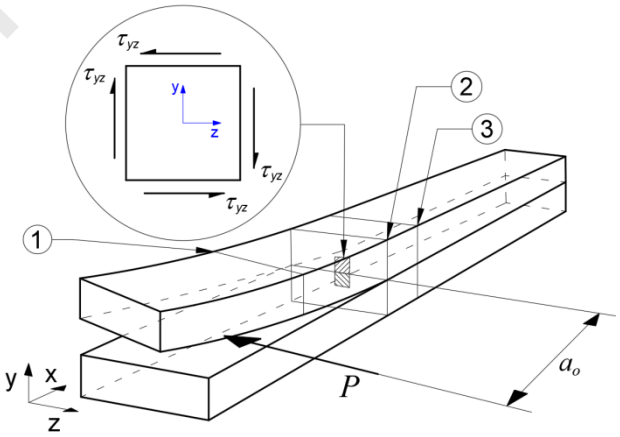

Fig. 24. Samples obtained near the crack front.

This micrograph shows intralaminar cracks at approximately 45° with respect to the midplane as were also observed by Czabaj et al. [20], [22], Johnston et al. [21] and Martin [14] for other test configurations.

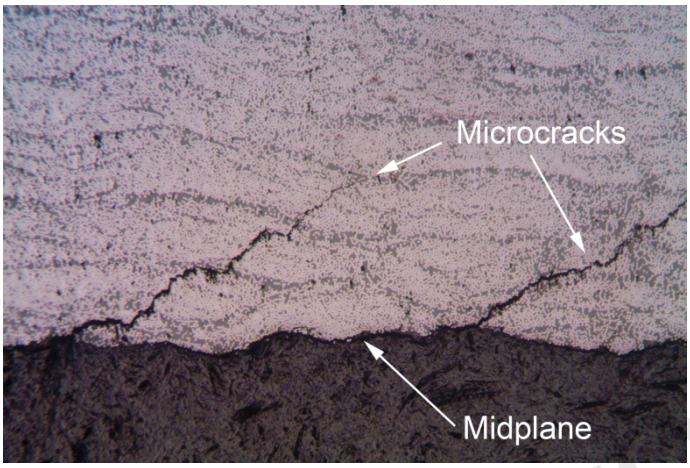

Fig. 25. Cracks near the crack front. Upper sublaminate x50.

As these authors found, these cracks seem to be produced by the resolved principal stress. Fig. 26 shows the stress state at one point near the crack front. This point is subjected to pure shear mode in the reference coordinates *xyz*. The maximum normal stress take place in a coordinate system rotated 45° with respect to the original *xyz* system (Fig. 26) where the shear stress becomes zero. Cracks are then formed perpendicular to the maximum traction stress.

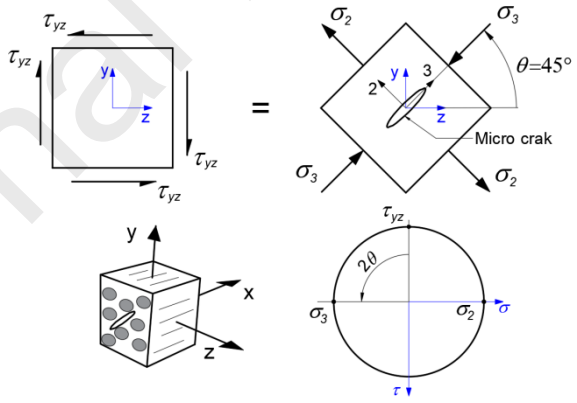

Fig. 26. Maximum normal stress at the crack front. In the Mohr circle, shear stress is plotted as positive downward.

This type of intralaminar cracks was also observed in section 3. In contrast, section 1 did not present these cracks.

6. Conclusion

In this work, the LHFB test for mode III characterization was analysed by means of FEM and optical microscopy.

Regarding the energy release rate distribution across the crack front, it was found that for samples with long initial crack lengths, pure mode III takes place mainly in the central part of the sample. In these samples, there is a significant contribution of mode II at the edges of the specimen.

As the initial crack length decreases, the load is applied closer to the crack tip, the bending moment decreases and, therefore, mode II contribution also decreases.

When the load is applied too close to the crack tip (the crack length is remarkably short), it exercises a local influence on the crack tip at the edge of the sample where the force is applied and mode III distribution loses its uniformity across the crack front.

When comparing analytical results with the total energy G_T obtained by FEM, the error between results is in the order of 33-36% for long initial crack lengths. In these type of samples, the average mode II contribution is in the range of 20-30% of the total energy. The error decreases to 17-7% as the initial crack length decreases to 5-1 mm. For small initial crack lengths, the average contribution of mode II decreases to less than 10% and so, G_T is nearly coincident with G_{III}. Mode I contribution is always negligible.

When comparing G analytical with G_{III} obtained by FEM, results were closer (4-23%)

Regarding the micromechanics of failure, intralaminar cracks, formed at 45° with respect to the midplane, were observed in planes parallel to the yz plane as other researchers did for other mode III test configurations. These cracks are probably produced by the resolved principal stress being perpendicular to the maximum traction stress.

It would be necessary to conduct additional research to try to contain these 45° intralaminar cracks and in this way have a greater approximation to a pure delamination process without additional mechanisms that could influence the global energy of fracture. On the other hand, other analytical formulations based, for example, in an experimental-numerical calibration of the compliance, could be used to try to improve the coincidence of G_T calculated by means of analytical and numerical methods.

Funding

This work was supported by the Spanish Ministry of Science, Innovation and Universities, within the framework of the research project RTI2018-095290-B-I00.

Research data for this article

Data will be made available on request

References

[1] Blackman BRK, Brunner AJ, Williams JG. Mode II fracture testing of composites: a new look at an old problem. Eng Fract Mech 2006;73:2443–55. doi:10.1016/j.engfracmech.2006.05.022.

[2] Todo M, Jar P-Y. Study of mode-I interlaminar crack growth in DCB specimens of fibre-reinforced composites. Compos Sci Technol 1998;58:105–18. doi:10.1016/S0266-3538(97)00102-4.

[3] Mollón V, Bonhomme J, Elmarakbi AM, Argüelles A, Viña J. Finite element modelling of mode i delamination specimens by means of implicit and explicit solvers. Polym Test 2012;31:404–10. doi:10.1016/j.polymertesting.2011.12.008.

[4] Mollón V, Bonhomme J, Viña J, Argüelles A, Fernández-Canteli A. Influence of the principal tensile stresses on delamination fracture mechanisms and their associated morphology for different loading modes in carbon/epoxy composites. Compos Part B Eng 2012;43:1676–80. doi:10.1016/j.compositesb.2011.07.018.

[5] ISO 15024. Fibre-reinforced plastic composites. Determination of mode I interlaminar fracture toughness, GIc, for unidirectionally reinforced materials 2001:1–24.

[6] ASTM D5528-13. Standard Test Method for Mode I Interlaminar Fracture Toughness of Unidirectional Fiber-Reinforced Polymer Matrix Composites. ASTM Int 2013;15.03:1–13. doi:10.1520/D5528.

[7] ASTM D7905/D7905M-14, ASTM D7905/D7905M-14. Standard Test Method for Determination of the Mode II Interlaminar Fracture Toughness of Unidirectional Fiber-Reinforced Polymer Matrix Composites. ASTM Int 2014;15.03:1–18. doi:10.1520/D7905.

[8] Boyano A, Mollón V, Bonhomme J, De Gracia J, Arrese A, Mujika F. Analytical and numerical approach of an End Notched Flexure test configuration with an inserted roller for promoting mixed mode I/II. Eng Fract Mech 2015;143:63–79. doi:10.1016/j.engfracmech.2015.06.031.

[9] Crews JH, Reeder JR. A mixed-mode bending apparatus for delamination testing. Hampton, Virginia 23665-5225: NASA; 1988.

[10] Benzeggagh ML, Kenane M. Measurement of Mixed-Mode Delamination Fracture Toughness of Unidirectional Glass / Epoxy Composites With Mixed-Mode Bending Apparatus. Compos Sci Technol 1996;56:439–49.

[11] ASTM D6671/D6671M – 13e1. Standard Test Method for Mixed Mode I-Mode II Interlaminar Fracture Toughness of Unidirectional Fiber Reinforced Polymer Matrix Composites. ASTM Int 2013:1–15. doi:10.1520/D6671.

[12] Szekrényes A. Interlaminar fracture analysis in the GI-GII-GIII plane using prestressed transparent composite beams. Compos Part A Appl Sci Manuf 2011;30:1655–69. doi:0.1177/0731684411418549.

[13] Donaldson SL. Mode III interlaminar fracture characterization of composite materials. Compos Sci Technol 1988;32:225–49. doi:10.1016/0266-3538(88)90022-X.

[14] Martin RH. Evaluation of the Split Cantilever Beam for Mode III Delamination Testing. Nasa Tech Memo 101562 1989.

[15] Becht GJ, Gillespie JW. Numerical and Experimental Evaluation of the Mode III lnterlaminar Fracture Toughness of Composite Materials. Polym Compos 1989;10:293–304. doi:10.1002/pc.750100505.

[16] Lee S. An Edge Crack Torsion Method for Mode III Delamination Fracture Testing. J Compos Technol Res 1993;15:193.201. doi:10.1520/CTR10369J. ISSN 0884-6804.

[17] Zhao D, Wang Y. Mode III fracture behavior of laminated composite with edge crack in

torsion. Theor Appl Fract Mech 1998;29:109–23. doi:http://dx.doi.org/10.1016/S0167-8442(98)00023-8.

[18] de Morais AB, Pereira AB, de Moura MFSF, Magalhães AG. Mode III interlaminar fracture of carbon/epoxy laminates using the edge crack torsion (ECT) test. Compos Sci Technol 2009;69:670–6. doi:10.1016/j.compscitech.2008.12.019.

[19] Ratcliffe JG. Characterization of the Edge Crack Torsion (ECT) Test for Mode III Fracture Toughness Measurement of Laminated Composites. NASA Tech Memo 2004.

[20] Czabaj MW, Ratcliffe JG, Davidson BD. Observation of intralaminar cracking in the edge crack torsion specimen. Eng Fract Mech 2014;120:1–14. doi:10.1016/j.engfracmech.2014.03.002.

[21] Johnston AL, Davidson BD, Simon KK. Assessment of split-beam-type tests for mode III delamination toughness determination. Int J Fract 2014;185:31–48. doi:10.1007/s10704-013-9897-1.

[22] Czabaj MW, Davidson BD, Ratcliffe JG. A Modified Edge Crack Torsion Test for Measurement of Mode III Fracture Toughness of Laminated Tape Composites. NASA Tech Rep Pap No 1706, NF1676L-25075 2016.

[23] Ge Y, Gong X, Hurez A, De Luycker E. Test methods for measuring pure mode III delamination toughness of composite. Polym Test 2016;55:261–8. doi:10.1016/j.polymertesting.2016.08.025.

[24] López-Menéndez A, Viña J, Argüelles A, Viña I, Rubiera S. Analysis of mode III interlaminar fracture toughness of laminated composites using a novel testing device. Eng Fract Mech 2017;173:55–63. doi:10.1016/j.engfracmech.2017.01.021.

[25] López-Menéndez A, Viña J, Argüelles A, Rubiera S, Mollón V. A new method for testing composite materials under mode III fracture. J Compos Mater 2016;50:3973–80. doi:10.1177/0021998316630395.

[26] López-Menéndez A, Viña J, Argüelles A, Lozano M. Validation of the Longitudinal Half Fixed Beam method for characterizing mode III delamination of composite laminates. Compos Struct 2016;147:74–81. doi:10.1016/j.compstruct.2016.03.019.

[27] Krueger R. Virtual crack closure technique: History, approach, and applications. Appl Mech Rev 2004;57:109. doi:10.1115/1.1595677.

[28] Mollón V, Bonhomme J, Elmarakbi AM, Argüelles A, Viña J. Finite element modelling of mode I delamination specimens by means of implicit and explicit solvers. Polym Test 2012;31:404–10. doi:10.1016/j.polymertesting.2011.12.008.

[29] Bonhomme J, Argüelles A, Viña J, Viña I. Numerical and experimental validation of computational models for mode I composite fracture failure. Comput Mater Sci 2009;45:993–8. doi:10.1016/j.commatsci.2009.01.005.